

This is the peer-reviewed version of the article:

Milikić, J., Vasić, M., Amaral, L., Cvjetićanin, N., Jugović, D., Hercigonja, R., Šljukić, B., 2018. NiA and NiX zeolites as bifunctional electrocatalysts for water splitting in alkaline media. International Journal of Hydrogen Energy 43, 18977–18991.

<https://doi.org/10.1016/j.ijhydene.2018.08.063>



This work is licensed under the

[Attribution-NonCommercial-NoDerivatives 4.0 International \(CC BY-NC-ND 4.0\)](#)

NiA and NiX zeolites as bifunctional electrocatalysts for water splitting in alkaline media

Jadranka Milikić^{a,f}, Milica Vasić^{a,f}, Luís Amaral^b, Nikola Cvjetićanin^a, Dragana Jugović^c, Radmila Hercigonja^a, Biljana Šljukić^{a,*}

^a Faculty of Physical Chemistry, University of Belgrade, Studentski trg 12–16, 11158
Belgrade, Serbia

^b Center of Physics and Engineering of Advanced Materials (CeFEMA), Instituto Superior
Técnico, Universidade de Lisboa, 1049-001 Lisbon, Portugal

^c Institute of Technical Sciences of SASA, Knez Mihailova 35/IV, Belgrade, Serbia
^f equally contributed

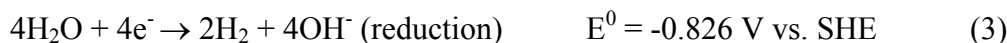
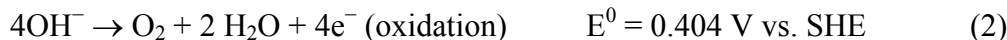
* corresponding author: E-mail: biljka@ffh.bg.ac.rs, Tel. +381 11 2187 133; Fax: +381 11
2187 133

Abstract: NiA and NiX zeolites were prepared and characterised using XRD, FTIR and SEM, and subsequently tested as electrodes for hydrogen (HER) and oxygen (OER) evolution reactions in alkaline media. Linear sweep voltammetry and chronoamperometry techniques showed that NiA has higher catalytic activity for these two reactions, as evidenced by higher current densities, which can be correlated with a higher weight fraction of Ni in this electrocatalyst than in the NiX and with its higher conductivity. HER and OER kinetic parameters, including Tafel slope, exchange current density and apparent activation energy were evaluated. Electrochemical impedance spectroscopy analysis yielded values of the resistance of the solution, charge transfer and mass transfer, as well as double layer capacitance and pseudo-capacitance of the working electrode, at different potentials and temperatures. Unlike the HER, during which the mass transfer resistance of the adsorbed intermediate is dominant in the case of NiA, the OER impedance response is controlled by the charge transfer process itself at the potentials of interest for these process. The overall resistance related to the HER is lower for NiA than for NiX.

Keywords: alkaline water electrolysis; oxygen evolution reaction; hydrogen evolution reaction; NiA zeolite; NiX zeolite.

1. INTRODUCTION

Alkaline water electrolysis (**Eq. 1**) is considered as a simple and clean method for hydrogen (and oxygen) production [1,2]. Still, this process is not thermodynamically favourable, requiring high quantity of energy for water molecule splitting [3]. Namely, oxygen evolution reaction (OER) (**Eq. 2**) proceeding at the anode and hydrogen evolution reaction (HER) (**Eq. 3**) proceeding at the cathode require large overpotential to proceed at reasonable rates [4,5]. These further results in high cost of alkaline water electrolysis process and high cost of produced hydrogen [6,7]. Therefore, it is necessary to design electrocatalysts with high activity for these two reactions, along with good electrical conductivity, large active surface area, electrochemical stability and selectivity, high corrosion resistance, and low cost [5,8–11].



In alkaline solutions, HER on a metallic electrode follows one of the two possible mechanisms - Volmer-Heyrovsky (**Eqs. 4** and **5**) or Volmer-Tafel (**Eqs. 4** and **6**) mechanism [12]:



where MH_{ads} is a hydrogen atom adsorbed on the electrode surface. The strength of the MH_{ads} bond determines the HER rate, with the best electrocatalysts exhibiting intermediate MH_{ads} bond strength values [13,14]. High catalytic activity towards HER is a characteristic of noble metals such as platinum, but their practical application is limited by their low abundance and high price [15,16]. On the other hand, nickel (Ni) is a promising electrode material for large-scale application since it has relatively low price and has shown good activity for HER [17–19]. Recently, attention has been directed towards improvement of HER activity of Ni-based electrocatalysts, including Ni alloying with other metals [20–24], non-metals or rare earth elements [25–29], fabrication in the form of foam [30] or nanostructured Ni composites [31–34], etc. The latest research is focused on Ni-sulphides (NiS , NiS_2 and Ni_3S_2) [35], phosphides (Ni_2P and Ni_5P_4) [36], nitrides (Ni_2N and Ni_3N) [37–39] and selenides [40] that have been shown to possess excellent activity for HER, with high current densities at low overpotentials (10 mA cm^{-2} at the overpotentials ranging from 49 to 474mV [16]).

The best electrocatalytic response towards OER is achieved for nanocomposites of precious metals, ruthenium and iridium, as they show the lowest OER overpotential, but they suffer from low stability in alkaline media [16,41]. Ni and its alloys exhibit lower electrocatalytic activity for OER, but they have long time stability in highly alkaline media (typically, concentrated KOH) and they are corrosion resistant [42–47]. OER on transition metal electrodes occurs at surface already covered by oxide layer. Namely, it has been observed that, during OER on Ni surface, NiO is firstly formed and then it is electrochemically oxidized to Ni₂O₃ [41]. Thus, Ni-based electrodes have a rest potential of oxide couple (Ni/NiO or NiO/Ni₂O₃) close to the equilibrium potential of the OER. Again, Ni sulphides (FeNiS₂) [48], phosphides (Ni₂P, Ni-Fe_xP and (Ni_{0.87}Fe_{0.13})₂P-Ni) [32,49], nitrides (Ni₃N/Ni) [50] and selenides (Ni₃Se₂ and Ni_xFe_{1-x}Se₂) [51,52], deliver high current density at low overpotentials.

Zeolites are recently finding application in electrochemistry area, in electroanalysis [53,54], as well as in electrochemical energy conversion and storage [55–59]. Thus, Pt-, Pd- and Ni-ion exchanged zeolites were tested as anode electrocatalysts in fuel cells for oxidation of fuels such as alcohols and borohydride [57,59–63]. These zeolites were also tested for HER [55] and OER [64]. There are more than 40 natural and 200 synthetic forms of zeolites [65,66] with basic structure made by three-dimensional combination of AlO and SiO tetrahedral [66]. These anionic groups have different negative charge ((AlO₄)⁻⁵ and (SiO₄)⁻⁴) which could be balanced by a positive ion (Na⁺¹, Ag⁺¹, Ni²⁺, Mn²⁺, Pt²⁺, Pd²⁺, etc.). The use of zeolites has a number of advantages, with some of them being good mechanical, thermal and chemical stability, and large surface areas [53,67].

In this work, two types of Ni²⁺ cation-exchanged zeolites, NiA and NiX, with different Si/Al ratio, were prepared. Subsequently, oxygen and hydrogen evolution reactions were studied at these two Ni zeolites in highly alkaline media by cyclic voltammetry (CV), linear sweep voltammetry (LSV), electrochemical impedance spectroscopy (EIS) and chronoamperometry (CA).

2. EXPERIMENTAL

Syntheses and characterization of Ni zeolite materials

Ni²⁺ cation-exchanged forms of NaX (Union Carbide) and NaA (BDH) zeolites used in this work were obtained by conventional ion-exchange procedure [54]. The composition of two

zeolites was determined by chemical analysis so that NiX and NiA zeolites are represented by the formula $\text{Na}_{23}\text{Ni}_{32}(\text{AlO}_2)_{87}(\text{SiO}_2)_{105}$ and $\text{Ni}_6(\text{AlO}_2)_{12}(\text{SiO}_2)_{12}$, respectively. The Ni zeolite samples were characterized by X-ray powder diffraction (XRPD), Fourier-transformed infrared spectroscopy (FTIR) and scanning electron microscopy (SEM) techniques. X-ray diffraction data were collected on a Philips PW 1050 diffractometer with Cu-K $\alpha_{1,2}$ radiation (Ni filter) at room temperature. Measurements were done in 2θ range of 5–80° with a scanning step width of 0.05° and time of 3 s per step. FTIR spectra of the powdered samples, dispersed in KBr and compressed into pellets, were recorded in 4000–400 cm^{-1} range at 64 scans per spectrum at 2 cm^{-1} resolution using Avatar 370FT-IR Spectrometer (Thermo Nicolet). The morphology of the zeolites was investigated using a JEOL JSM 7001F scanning electron microscope.

Electrical conductivity measurements were done using Precision LCR Meter (LCR-6100) at the frequency of 1 kHz. Conductivity was measured directly in the die (with hard plastic interior and steel exterior) at 125 kPa.

Preparation of the working electrodes

In order to prepare catalytic inks, a mixture of zeolite (NiA or NiX, 4 mg) and Vulcan carbon black (1 mg) was dispersed in 125 μl of polyvinylidene fluoride (PVDF) solution (2 wt.% PVDF in N-methyl-2-pyrrolidone) and homogenised in an ultrasonic bath for 30 min. Subsequently, 10 μL of the ink was deposited onto glassy carbon substrates, and then dried at 110 °C overnight to make the working electrodes.

Electrochemical measurements

All measurements were done using Gamry PCI4/750 Potentiostat/Galvanostat in a one-compartment cell of 50 ml volume with 1 M KOH as electrolyte, and with carbon rod as counter electrode and saturated calomel as reference electrode (SCE). The values of electrode potential given in the paper are presented relative to the reversible hydrogen electrode (RHE). Current densities were calculated by dividing the recorded currents by the geometric surface area of the electrode.

Cyclic voltammetry (CV) characterisation of the zeolites was performed in the deareated 1 M KOH in the potential range from 0.08 to 1.85 V at a scan rates ranging from 2 to 100 mV s^{-1} , at room temperature. Prior to recording HER polarization curves, the oxides on the electrode surface were reduced by a linear scan voltammetry (LSV) from the OCP to -0.43 V at a rate of 10 mV s^{-1} , followed by holding the electrode at the potential of -0.45 V for 45 s. HER

polarization curves were recorded from the open circuit potential (OCP) to -0.43 V at 2 mV s⁻¹. OER polarisation curves were recorded from the OCP to 2.27 V at a scan rate of 10 mV s⁻¹. OER polarisation curves were also recorded using rotating disk electrode (RDE) at rotation rate of 1200 rpm which was adjusted using a Pine AFCPRB rotator. The polarization curves were also recorded at different temperatures from 25 to 85 °C, adjusting the temperature by water circulation using a Haaeke F3 bath. Chronoamperometry (CA) measurements were performed at the constant potential for 1 h, at room temperature. Electrochemical impedance spectroscopy (EIS) measurements were conducted in the frequency range of 100 kHz to 0.1 Hz, with 5 mV amplitude, at different potentials.

3. RESULTS AND DISCUSSION

Characterization of Ni zeolites

The crystal structure of the synthesized powders was confirmed by X-ray powder diffraction. All diffraction peaks of NiA powder can be ascribed to cubic $Fm\bar{3}c$ space group (No. 226) by comparison with diffraction card PDF2 No. 73-2340. The most intense peaks of NiA powder are indexed according to this space group, **Figure 1A**. There are no additional peaks that can be ascribed to some other phase. Similarly, by comparison with PDF2 card No. 39-1380, all diffraction peaks of NiX powder can be ascribed to cubic $Fd\bar{3}m$ space group (No. 227). **Figure 1B** shows diffraction pattern of NiX with the most intense peaks indexed according to $Fd\bar{3}m$ space group. Lattice parameters were determined by using the Le Bail's whole profile unit cell refinement [54] within FullProf program and the obtained values are 24.9170 and 24.5027 Å for NiX and NiA samples, respectively. **Figure 1A** also reveals the broadening of several diffraction peaks, namely those at 2θ angle of approximately 11, 24 and 35°, which originates from the distortion of the zeolite crystal lattice during the ion exchange. In the case of sample NiX, broad peaks are harder to be observed. Using the X-ray Line Profile Fitting Program (XFIT) with a Fundamental Parameters convolution approach to generating line profiles [68], the coherent domain sizes of the synthesized powders was calculated to be 47 and 30 nm for NiX and NiA, respectively. This difference in the coherent domain sizes is in agreement with the more distorted structure observed for NiA sample.

Presence of the Ni²⁺ ions as the charge balance cations in the NiA promotes the instability and hydrolysis of the zeolite framework. Namely, the most or all of the Ni²⁺ ions in hydrated NiA

are typically in the form of the aqueous complex, $\text{Ni}(\text{H}_2\text{O})_6^{2+}$, so that Ni^{2+} ions in NiA zeolite retain an aqueous coordination sphere and do not coordinate directly to the anionic zeolite framework, as the most of the other charge balance cations [68]. Consequently, there is a large charge separation between charge balance cations and the zeolite framework. Coordinated water molecules dissociate and provide H^+ ions which can then associate with the zeolite framework and effectively neutralize the zeolite framework. This process does not directly disrupt the crystallinity of the zeolite framework, but the basic sites near the Al^{3+} ions have also been produced by the hydrolysis reaction enabling $\text{Al}(\text{OH})_3$ abstraction from the zeolite and thus causing the disruption of the framework structure. An increase in the number of metal ions in the zeolite would favour this reaction by the production of more protons.

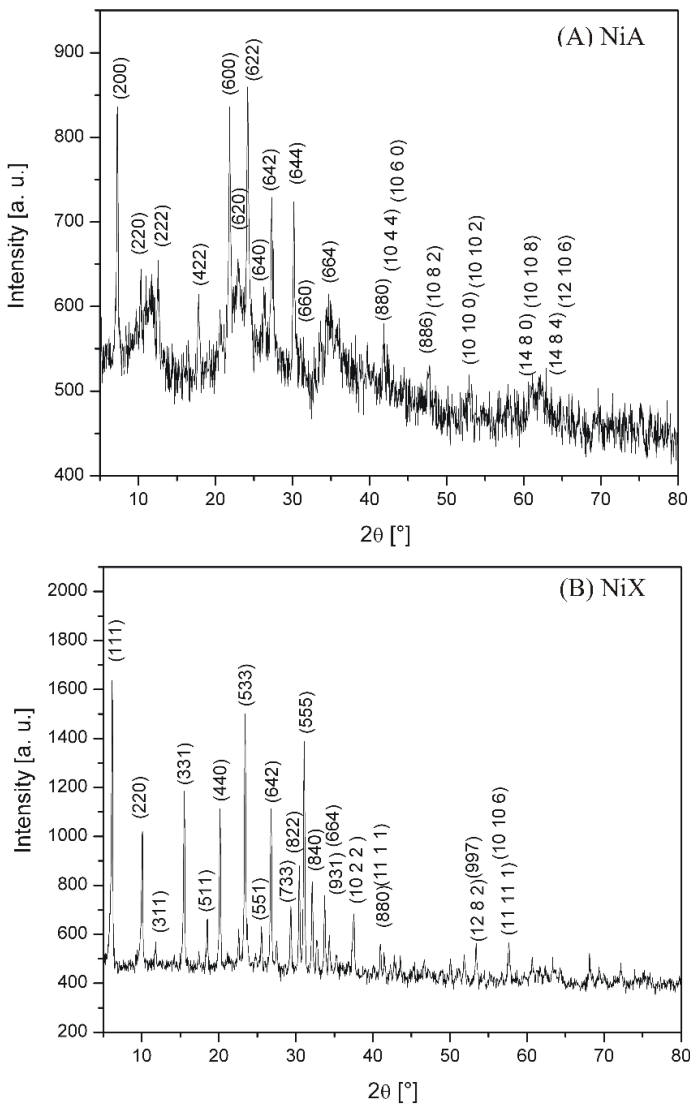


Figure 1. XRD patterns of NiA (A) and NiX (B) zeolite, with the most intense peaks indexed according to $Fm\bar{3}c$ and $Fd\bar{3}m$ space group, respectively.

FTIR analysis of NiA confirmed the collapse of the long-range order and the amorphisation of its structure. The FTIR spectra of NiA and NiX zeolites in mid-infrared region, at room temperature, are presented in **Figure 2A**. The main structural absorption bands of FTIR spectra were observed at 980 and 1015 cm⁻¹ for NiX, and NiA, respectively [54,69,70], with these bands corresponding to the stretching vibrations of Si-O and Al-O bonds, respectively. In the NiX spectrum, a shoulder was noticed at 1072 cm⁻¹ which could correspond to Si-O-Si vibrations [54,69,70]. The absorption internal Si-O-Al bonds appeared at 427 and 449 cm⁻¹ for NiA and NiX zeolites, respectively [70]. Two absorption bands of NiX zeolite at 914 and 748 cm⁻¹ could be associated with the stretching of Al-O bonds [54]. In addition, two bands were detected in the absorption region from 700 to 500 cm⁻¹ in spectrum of NiX zeolite, first band at 682 cm⁻¹ attributed to the double rings stretching and second, main structural sensitive band in the spectrum of faujasite, at 559 cm⁻¹ which corresponds to the double six-membered rings vibration stretching. Also, in the same absorption region of spectrum of NiA zeolite, two bands appeared at 677 and 545 cm⁻¹. They could be attributed to the single six- and double four-membered rings stretching, respectively [69,71].

Morphological properties of NiA and NiX zeolites were determined by SEM with the micrographs of the analysed zeolites expected to be different [54,72]. Namely, the particles of NiA zeolite appeared as well-defined edge-truncated cubes (**Figure 2B**), while NiX showed aggregates of octahedral crystals (**Figure 2C**) [72]. The crystals of NiA and NiX zeolites were observed to be about 3 µm in diameter.

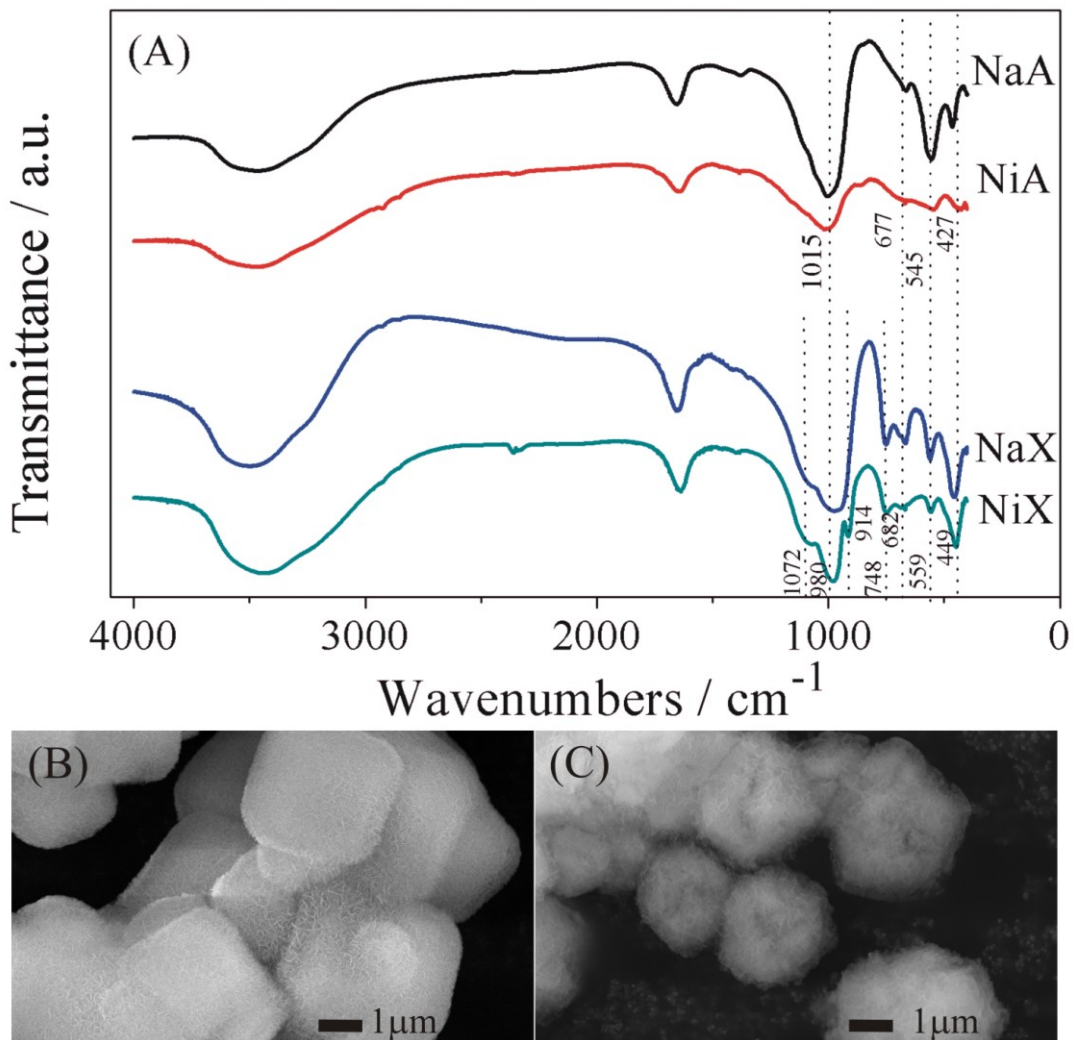


Figure 2. FTIR absorption spectra (A) and SEM images of NiA (B) and NiX (C) zeolites.

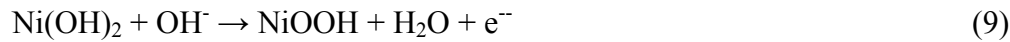
NiA zeolite ($4.4 \times 10^{-6} \text{ S cm}^{-1}$) showed two orders of magnitude higher electrical conductivity compared to NiX zeolite ($7.7 \times 10^{-8} \text{ S cm}^{-1}$) at room temperature, possibly due to higher amount of Ni in the former. Furthermore, zeolites' conductivity is considered as ionic, with a negligible electronic contribution. Ion conductivity of zeolite is related with the diffusion of charge balance cations through the zeolite channels. Hydrated zeolites are also proton conductors and OH^- ion conductors. The dissociation of water in the zeolite channels occurs similarly to that in free water, supplying OH^- and H_3O^+ ions as charge carriers, moving by molecular jumps and proton transfer. One could suggest that cation mobility in the channels of crystalline structure should be higher than that in the amorphous phase, in which the channels are partially or completely distorted and damaged. However, the amorphisation could be responsible for the anomalous increase in electrical conductivity of hydrated zeolites

[73]. The amorphisation creates new pathways allowing the higher mobility of the cations than that through the zeolite channels, which lead to increase of conductivity.

Still, as both NiA and NiX conductivity is measured to be low for practical applications, two zeolites were mixed with Vulcan XC 72 for electrode preparation, as described in the *Experimental* section.

Electrochemical characterization of Ni zeolites

Electrochemical characterisation of NiA and NiX electrodes was performed by CV in 1 M KOH solution purged with nitrogen (N_2) at room temperature, **Figure 3**. Three CVs were recorded at each scan rates with no changes in the curves shape nor current density values being observed. According to the literature, several processes are expected to occur in the anodic direction in alkaline solutions: formation of nickel oxide (NiO) (**Eq. 7**) or nickel hydroxide ($Ni(OH)_2$) (**Eq. 8**), followed by transformation of α - to β - $Ni(OH)_2$, and then β - $Ni(OH)_2$ to nickel oxyhydroxide ($NiOOH$) (**Eq. 9**) [74,75].



These processes give a rise to a peak in the anodic direction at around 1.5 V, while on the cathodic scan, reduction of Ni^{3+} to Ni^{2+} is manifested as a peak at 1.35 V. A shoulder on the reduction scan at around 1.25 V, observed only for NiA, can be ascribed to the Ni^{2+} to Ni^0 conversion. Additionally, the CVs of both electrodes exhibit a broad cathodic peak at around 0.75 V, which corresponds to the reduction of oxygen which remained within the zeolite pores, in gaseous or dissolved state [57,76]. However, higher current responses in the regions of redox processes are observed in the case of the NiA electrode, most likely due to the higher Ni content in this material (19.68 wt.% of in NiA vs. 13.57 wt.% of Ni in NiX) and due to its higher conductivity.

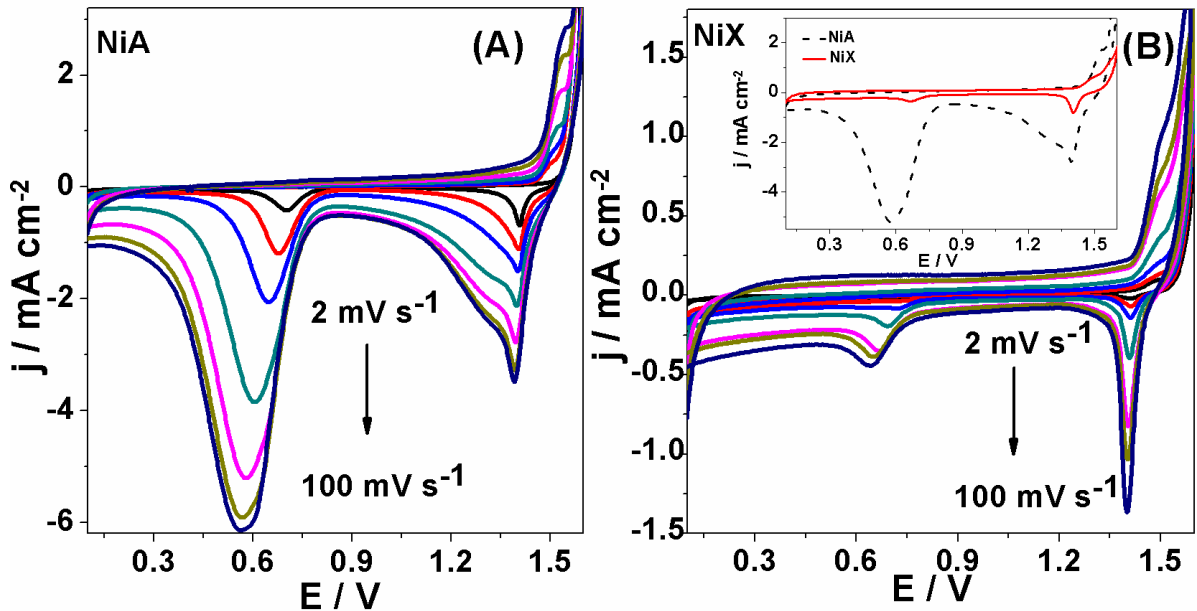


Figure 3. Cyclic voltammograms of NiA (A) and NiX (B) electrodes at room temperature in N_2 -saturated 1 M KOH at different scan rates with CVs of two zeolites at scan rate of 50 mV s^{-1} in inset.

The electrochemical characterisation of NiA and NiX reveals important information about their pseudocapacitive characteristics that are vital for their performance for both the HER and OER as H/O adsorption (underpotential deposition) on the electrocatalyst's surface is precondition for HER/OER. More pronounced pseudocapacitive behaviour is accompanied by better HER/OER electrocatalytic performance. Namely, high pseudocapacitance shows the presence of large number of active sites which can participate in the adsorption processes in the H/O adsorption region. CVs at different scan rates reveal rate capability of NiA and NiX, i.e., how efficiently they can adsorb a significant H/O amount and desorb with a high coulombic efficiency. The ideal pseudocapacitive behaviour evidenced by a rectangular shape of CV curves, is directly associated with higher electrocatalytic activity for HER as can be characterised by a lower overpotential. Evaluation of the capacitance of the two studied zeolites shows significantly higher values of capacitance were determined for NiA at all scan rates. Moreover, sharp peak at ca. 1.4 V in case of NiX indicate absence of pseudocapacitance in the OER region in case of this zeolite.

Of course, the electrocatalytic reactivity of the active sites depends on their accessibility and their oxidation state. Thus, amorphous structure of NiA, its porosity and permeability, contribute to the formation of active sites with minimum overpotential. This might be

especially important in the case of the OER that is not ideally a surface reaction and it proceeds within a thin layer (e.g., 10 nm) of the electrocatalyst metal oxide [77].

As for the active sites' oxidation state, for case of OER, they should be in their high oxidation states, that occurs at potentials lower than that of OER in case of pronounced pseudocapacitive characteristics of an electrocatalyst.

Study of HER at NiA and NiX zeolite electrodes

HER polarization curves of NiA and NiX were recorded in 1 M KOH solution in the potential range from the OCP to -0.43 V. The OCP values at 25 °C amounted to 0.878 and 0.866 V for NiA and NiX, respectively. The polarization curves at 25 °C revealed that the process followed by visible bubble formation starts at around 0.5 V, representing the HER, **Figure 4A**. NiA demonstrated better activity for HER than NiX, most likely due to higher weight fraction of Ni in the NiA and its higher conductivity. This metal is very attractive as an electrode material for HER, since the strength of the bond of an adsorbed proton to Ni surface is intermediate, making Ni the most active pure metal among the non-noble candidates [78].

According to Tafel equation, :

$$\eta = a + b \log j = \frac{2.3RT}{\alpha F} \log j_0 - \frac{2.3RT}{\alpha F} \log j \quad (10)$$

Tafel plots were constructed (**Figure 4A inset**), where η is the overpotential, j is the current density, R is the universal gas constant, T is the temperature, F is Faraday's constant, α is the charge transfer coefficient, b is the Tafel slope, j_0 is the exchange current density. NiA gave lower Tafel slope value of 551 mV dec⁻¹ compared to value of 857 mV dec⁻¹ evaluated for NiX, **Table 1**. However, these values of Tafel slope are much higher than those usual for HER on Ni-based electrodes in alkaline media, **Table 2** [24,26–28,33,79–82]. The slopes of Tafel plots obtained from the data recorded at 45 °C are lower than those obtained at 25 °C, but still quite high, **Table 1**. Such high values of Tafel slope indicate hindered electron transfer through the material [83]. There are various factors influencing the electrode performance, such as crystal and electronic structure of the material, its morphology, surface coverage by adsorbed intermediates, the presence of surface oxides, etc [33,83,84] According to Soares et al. [85], hydride formation at active Ni cathode surfaces changes the HER pathway to a condition in which hydrogen evolution is limited by the desorption through recombination, beside decreasing the active Ni area, giving Tafel slopes of 200 - 1000 mV dec⁻¹. Hydride formation and decomposition rates depend strongly on temperature, including more rapid decomposition at higher temperature [85].

On the other hand, the j_0 values obtained for both electrodes are of the same order of magnitude or even higher than the j_0 values of most of other Ni-based electrodes in alkaline media, **Tables 1** and **2**. However, high specific surface area of the electrocatalyst support results in the high ratio between real and geometric surface area of the supported electrocatalyst. Consequently, the number of active sites for the supported electrocatalyst is higher than for the electrocatalysts without such support, as well as j , provided that geometric surface area is used for determination of j .

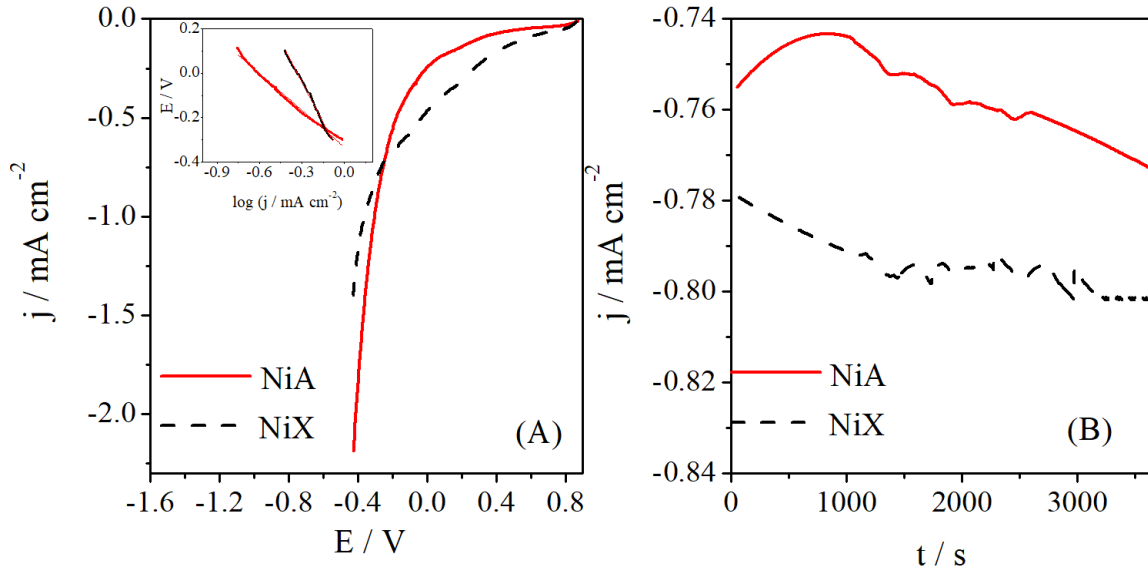


Figure 4. HER polarization curves of NiA and NiX at 25 °C with corresponding Tafel plots in inset (A). HER chronoamperometric curves of two electrodes at the constant potential of -0.33 V at 25 °C (B). All measurements carried out in 1 M KOH.

Table 1. HER Tafel slopes and exchange current densities of NiA and NiX electrodes at 25 and 45 °C.

| Temperature / °C | Electrode | b / mV dec ⁻¹ | j ₀ / mA cm ⁻² |
|------------------|-----------|--------------------------|--------------------------------------|
| 25 | NiA | 551 ± 3 | 0.261 ± 0.004 |
| | NiX | 857 ± 1 | 0.580 ± 0.005 |
| 45 | NiA | 494 ± 1 | 0.449 ± 0.001 |
| | NiX | 481 ± 4 | 0.280 ± 0.001 |

Table 2. Parameters of HER activity of some Ni-based electrocatalysts in alkaline solutions at 25 °C.

| Electrocatalyst | Electrolyte | b / mV dec ⁻¹ | j ₀ / mA cm ⁻² | Ref. |
|--------------------|-------------|--------------------------|--------------------------------------|------|
| Polycrystalline Ni | 1 M NaOH | 115 | 1.8×10 ⁻³ | [82] |
| Ni modified by | 0.5 M KOH | 191 | - | [24] |

| mechanical polishing | | | | |
|--|----------|---------|---------------------------|-------|
| MoNi | 1 M NaOH | 132-148 | 0.013-0.079 | [80] |
| NiAlMo | 1 M KOH | 70-180 | 15-166 | [79]] |
| NiP-TiO₂ | 5 M KOH | 197 | 1.43 | [81] |
| NiLa | 1 M NaOH | 170-198 | (4-12.6)×10 ⁻⁵ | [28] |
| NiCe | 1 M NaOH | 151-214 | (4-50)×10 ⁻⁶ | [28] |
| Ni_{0.95}Ce_{0.05} | 8 M KOH | 126 | 1.35 × 10 ⁻³ | [27]. |
| Ni_{0.95}Dy_{0.05} | 8 M KOH | 101 | 1.45×10 ⁻³ | [26] |
| Ni_{0.95}Sm_{0.05} | 8 M KOH | 74 | 1.57×10 ⁻³ | [26] |
| Ni | 8 M KOH | 103 | 1.15×10 ⁻³ | [27] |
| Ni foam | 8 M KOH | 109 | 3.3×10 ⁻³ | [30] |
| NiCu foam | 8 M KOH | 131 | 453×10 ⁻³ | [30] |
| NiO-Ni attached to carbon nanotubes | 1 M KOH | 82 | - | [40] |

The stability of the activity of NiA and NiX electrodes for HER was examined by chronoamperometry in 1 M KOH solution, at the constant potential of -0.33 V for 1 h. The electrodes exhibited relatively good stability, with a slight increase in current density during the measurements, **Figure 4B**. Higher current density was observed in the case of NiA electrode, as a result of its better activity for HER, which is in agreement with the data obtained by other electrochemical methods.

The HER at both the electrodes was also studied by EIS. **Figure 5** presents the Nyquist and Bode plots at several temperatures at NiA and NiX zeolites, under an applied potential of -0.33 V. The intersection of the spectra with the Z' axis at high frequency in the Nyquist plots in **Figure 5A,B** is equal to the sum of the resistances of the wiring, the electrode material and the electrolyte [86,87]. Additionally, two main relaxations are seen, which are identifiable by the well-resolved arcs in the Nyquist plots (**Figure 5A,B**) as well as by the separated peaks in the Bode plots of **Figure 5C,D**. A high frequency semi-circle can be seen in the insets in **Figure 5A,B**, while the largest arc can be observed at low frequencies. The arc diameter regarding both relaxations seem to change with the temperature in the case of NiA, while in the case of NiX the arcs of the high frequency relaxation show no effect of the temperature.

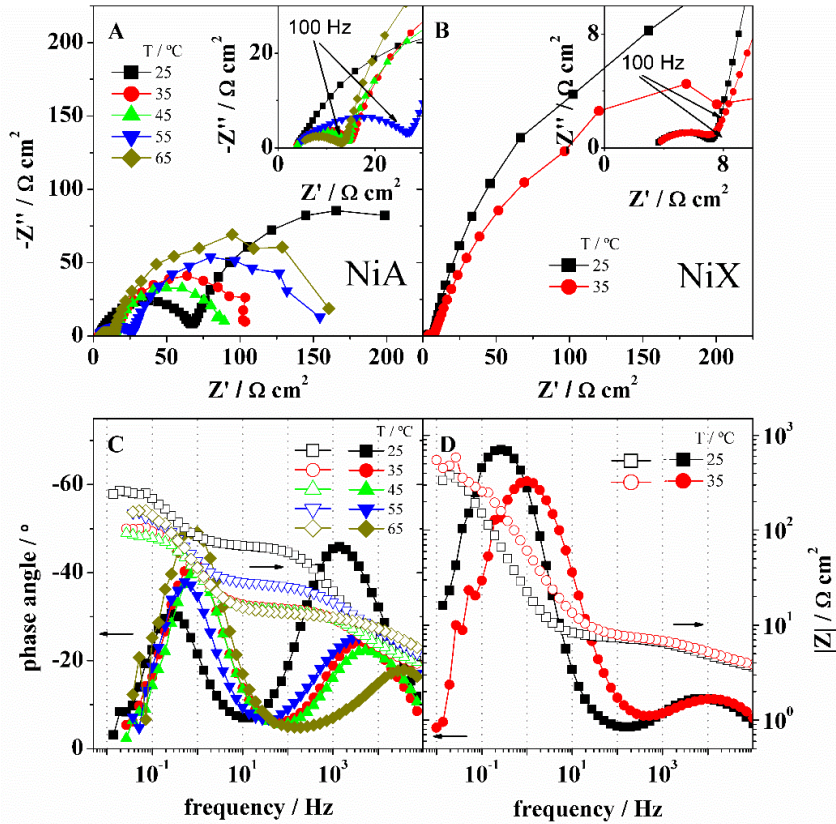


Figure 5. Nyquist (A, B) and Bode (C, D) plots at several temperatures for the HER at NiA (A, C) and NiX (B, D) electrocatalysts, under an applied potential of -0.33 V.

In the Bode plots regarding NiA (**Figure 5C**) it may be seen that the peaks in the phase angle are both well-defined and of comparable height, with the low-frequency peak increasing and the high frequency one decreasing with increasing temperature. The peaks and the transitions between them are shifted to higher frequencies with the increasing of temperature.

In the case of NiX, **Figure 5D**, the peak at high frequency does not change with the temperature and shows much lower height than that at low frequencies, meaning that the high frequency relaxation presents lower phase angles. This is accompanied by somehow depressed arcs in the Nyquist plots for this relaxation, occurring at slightly higher frequencies than in the case of NiA, as may be seen in the inset of **Figure 5B**. The flattening of the arcs is observed in the high frequency relaxation of both electrocatalysts, more evident in the case of NiX, and may be related to the inhomogeneity of the electrodes surface, due to the porous nature of the zeolite structure.

Figure 6 presents Nyquist and Bode plots at 25 °C for several applied potentials for both electrocatalysts. It can be observed that, as expected, the overall impedance decreases with increasing applied potential in both cases. The general characteristics of the plots are similar

to those described regarding **Figure 5**, generally showing two relaxations (with the exception of NiA at the OCP, **Figure 6A**, in which the high frequency one seems absent). The applied potential has an effect on both relaxations in the case of NiA, while NiX shows again clearly depressed arcs at high frequencies (inset of **Figure 6B**), independent of the applied potential, as is the frequency of the corresponding peaks in the Bode plots, **Figure 6D**. On the other hand, there is some effect of the applied potential on the low-frequency peak of the Bode plots in the case of NiX and on both peaks in the case of NiA (**Figure 6C**).

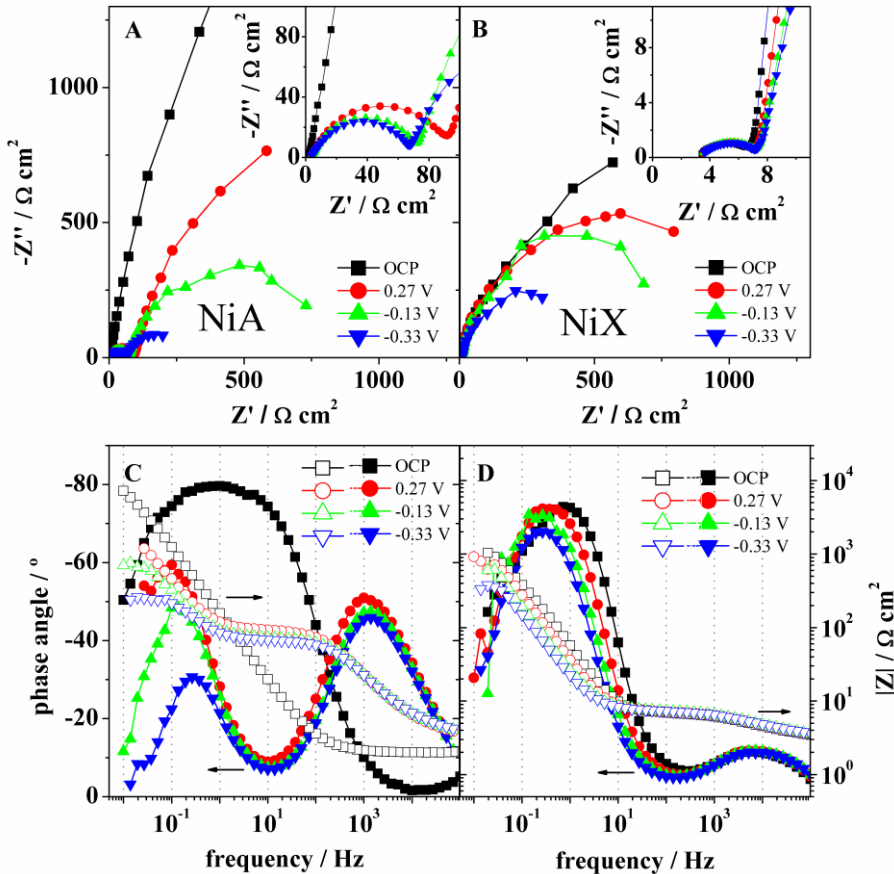


Figure 6. Nyquist (A, B) and Bode (C, D) plots at several applied potentials for the HER at NiA (A, C) and NiX (B, D) electrocatalysts, at 25 °C.

Considering the above described analysis, the impedance data was interpreted using the equivalent circuits in **Figure 7**. In order to increase the quality of the fittings, constant phase elements (CPE) were used in substitution of pure capacitors. CPE elements are usually used in the interpretation of impedance spectra to account for surface heterogeneity of real systems or a distribution of time constants on the electrode surface [88,89].

A modified version of the well-known equivalent electric circuit of Armstrong and Henderson [90–93], comprising two time constants in parallel, is presented in **Figure 7A**, where R_s is the

resistance of the solution, R_s is the charge transfer resistance related with the reaction at the working electrode, CPE_1 is related with the double layer capacitance of the working electrode, R_2 is the mass transfer resistance of the adsorbed intermediate H_{ads} , also known as pseudo-resistance, and CPE_2 describes the pseudo-capacitance of the working electrode. This equivalent circuit is normally used when the two relaxations are dependent on the potential, and therefore, related to the HER [94], as in the case of the HER at NiA. On the other hand, **Figure 7B** presents a two-time constant equivalent circuit with the two R-CPE elements in series, which has been used to model the HER when one of the relaxations is related to the HER kinetics and the other one is independent of the potential, and therefore not associated with the HER processes, but with the porosity of the electrode surface [94]. Therefore, this equivalent circuit was selected to model the HER at the NiX electrocatalyst.

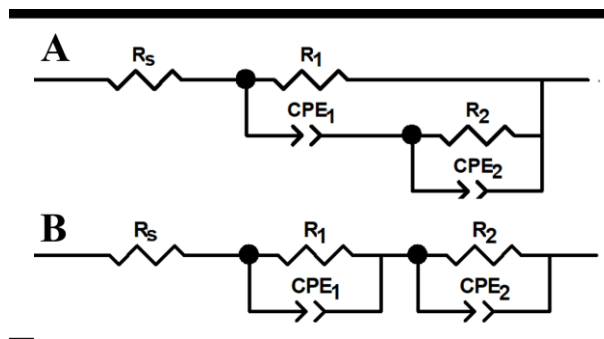


Figure 7. Two time constants equivalent circuits used to fit the impedance data of the HER on the NiA and NiX zeolites with two R-CPE elements (A) in parallel, and (B) in series.

The parameters obtained from fitting the data in **Figure 5** with the equivalent circuits in **Figure 7** are presented in **Table 3**. It may be seen that R_s is coarsely between 3 and 4 $\Omega \text{ cm}^2$ in both cases, slightly and systematically decreasing with the increase of temperature. This is in agreement with a slight increase of the conductivity of the electrolyte with the increasing temperature, as well as with some increase in the ease of bubble removal from the solution [95].

In the case of NiA, the charge transfer resistance, R_1 , seems to decrease with the temperature with most of the values roughly around 11-12 $\Omega \text{ cm}^2$. The resistance R_2 , related with the adsorbed hydrogen, seems to have a minimum at 45 °C, showing a value around 75 $\Omega \text{ cm}^2$. By its turn, NiX shows two-fold lower values for the high frequency resistance, R_1 , related with the porosity, which shows no effect of the temperature in the measured range. The charge

transfer resistance, R_2 in the case of NiX, decrease with the temperature, presenting values several times higher than those observed for NiA at the studied temperatures.

Regarding the capacitance in the case of NiA, C_1 shows values of the order of 10^{-6} F cm $^{-2}$, in the range of expected values for the capacitance of the double layer [86,91,96], slightly decreasing with increasing temperature. For the pseudo-capacitance, C_2 , higher values of the order of 10^{-3} F cm $^{-2}$ were obtained, in agreement with previously reported values [55,86,90], with no apparent dependence on the temperature. In the case of NiX, the capacitance associated with both the high and low frequency relaxations revealed values similar to those obtained for NiA.

Table 3. Parameters obtained from the EIS data at different temperatures for the HER at NiA and NiX electrocatalysts, at an applied potential of -0.33 V.

| T / °C | R_s / Ω cm 2 | R_1 / Ω cm 2 | C_1 / F cm $^{-2}$ | R_2 / Ω cm 2 | C_2 / F cm $^{-2}$ |
|------------|-------------------|-------------------|----------------------|-------------------|----------------------|
| NiA | | | | | |
| 25 | 4.0 | 67.0 ± 0.5 | 9.1×10^{-6} | 196.8 ± 6.4 | 5.8×10^{-3} |
| 35 | 3.6 | 12.1 ± 0.1 | 8.3×10^{-6} | 93.1 ± 0.7 | 6.0×10^{-3} |
| 45 | 3.6 | 11.5 ± 0.1 | 6.6×10^{-6} | 75.4 ± 0.5 | 6.0×10^{-3} |
| 55 | 3.5 | 25.9 ± 0.2 | 6.3×10^{-6} | 117.6 ± 1.6 | 5.6×10^{-3} |
| 65 | 3.1 | 10.9 ± 0.3 | 1.3×10^{-6} | 154.9 ± 2.3 | 5.2×10^{-3} |
| NiX | | | | | |
| 25 | 3.3 | 4.3 ± 0.1 | 9.3×10^{-6} | 563 ± 13 | 1.2×10^{-2} |
| 35 | 3.3 | 4.4 ± 0.1 | 6.0×10^{-6} | 463 ± 6 | 4.1×10^{-3} |

Table 4 presents the parameters obtained from the fitting of the impedance data at 25 °C for several applied potentials for both electrocatalysts, as shown in **Figure 6**, using the previously described equivalent circuits in **Figure 7A** for NiA and **Figure 7B** for NiX.

Table 4. Parameters obtained from the EIS data at different applied potentials for the HER at NiA and NiX electrocatalysts, at 25 °C.

| E_{applied} / V | R_s / Ω cm 2 | R_1 / Ω cm 2 | C_1 / F cm $^{-2}$ | R_2 / Ω cm 2 | C_2 / F cm $^{-2}$ |
|--------------------------|-------------------|-------------------|----------------------|-------------------|----------------------|
| NiA | | | | | |
| 0.27 | 3.7 | 93.3 ± 0.6 | 9.8×10^{-6} | 2271 ± 102 | 4.4×10^{-3} |
| -0.13 | 3.9 | 71.7 ± 0.5 | 8.8×10^{-6} | 745 ± 48 | 5.5×10^{-3} |
| -0.33 | 4.0 | 67.0 ± 0.5 | 9.1×10^{-6} | 197 ± 6 | 5.8×10^{-3} |
| NiX | | | | | |
| 0.27 | 3.3 | 4.2 ± 0.1 | 1.0×10^{-5} | 1099 ± 10 | 6.0×10^{-3} |

| | | | | | |
|-------|-----|---------------|----------------------|--------------|----------------------|
| -0.13 | 3.2 | 4.4 ± 0.1 | 9.6×10^{-6} | 900 ± 22 | 9.4×10^{-3} |
| -0.33 | 3.3 | 4.3 ± 0.1 | 9.3×10^{-6} | 563 ± 13 | 1.2×10^{-2} |

The values obtained for R_s are similar in both cases and equivalent to those presented in **Table 3**. An increasing trend of this resistance with the applied potential may be observed, which is probably related with the increasing amount of bubbles in the electrolyte. Regarding the HER related resistances, it can be seen that the charge transfer resistance (R_1 in the case of NiA and R_2 in the case of NiX) is much lower for NiA than for NiX, showing a decreasing trend with increasing applied potential in both cases. The pseudo-resistance, R_2 in the case of NiA, clearly decreases with the increase of the applied potential.

Considering the HER related resistances, the sum of R_1 and R_2 regarding NiA and only R_2 in the case of NiX, it may be seen that they are lower for NiA at high applied potentials, the potentials of interest for the HER, which suggests higher HER activity of this electrocatalyst in comparison with NiX.

The double layer capacitance, C_1 , shows again values of the order of $10^{-6} \text{ F cm}^{-2}$ for NiA, nearly independent of the applied potential. In agreement with the values presented above, C_2 generally shows values of higher magnitude of $10^{-3} \text{ F cm}^{-2}$ in both cases, slightly increasing as the applied potential becomes more negative. For NiX, despite the different models used, the capacitance values obtained for both the high and low frequency relaxations revealed to be similar to those obtained for NiA.

Study of OER at NiA and NiX zeolite electrodes

OER polarization curves of NiX and NiA recorded in 1 M KOH from the OCP to 2.27 V at scan rate of 10 mV s^{-1} and rotation rate of 1600 rpm are shown in **Figure 8A**. It was observed that during OER, NiA zeolite gave a significantly higher value of current density compared to NiX. Thus, NiA gave five times higher current density (21 mA cm^{-2}) than NiX (4 mA cm^{-2}) at 2.27 V during OER. Tafel slopes for low overpotential region of NiA and NiX were calculated (**Eq. 10**) from the slopes of E vs. $\log(j)$ plots (**Figure 8A, inset**) of polarization curves in 1 M KOH at 1600 rpm. OER Tafel slopes were found to be 842 mV dec^{-1} for NiX and 463 mV dec^{-1} for NiA, with these values being higher than literature values reported for similar Ni samples [97,98]. Still, value of 437 mV dec^{-1} was reported for OER at Ni foam [99] as well as value of ca. 503 mV dec^{-1} for OER at Ni foam modified with Pt/C [100], a value somewhat higher than the value obtained for NiA sample. Furthermore, OER Tafel slope at

NiA was observed to decrease with an increase of temperature; for instance, value of 356 mV dec⁻¹ was evaluated at 45 °C. Namely, OER polarisation curves were also attained at different temperatures in the range from 25 to 85 °C (not shown). With increasing temperature, slight increase in instability of NiA and NiX was noticed, due to formation of gas bubbles. Higher current densities were obtained with increasing temperature up to 55 °C. These data were used for calculating apparent activation energy E_a^{app} by Arrhenius equation (Eq. 11) [27]:

$$\frac{\partial \log j}{\partial (1/T)} = \frac{E_a^{\text{app}}}{R} \quad (11)$$

where R is the universal gas constant (8.314 JK⁻¹ mol⁻¹). The values of OER E_a^{app} on NiA and NiX were determined to be 18.2 and 18.6 kJ mol⁻¹, respectively. E_a^{app} values reported in the literature for OER on different Ni-based electrodes were between 55 [28] and 71 kJ mol⁻¹ [65]. Hence, OER at NiA and NiX proceeds with lower E_a^{app} than those reported in the literature.

Chronoamperometric test of stability of NiA and NiX (**Figure 8B**) in strongly oxidising conditions was carried out in 1 M KOH at 1.75 V for 3600 s at 25 °C. NiA gave significantly higher OER current density than NiX in accordance with the OER LSV results. Current density was observed to decrease with time, reaching stable value after 200 s. Thus, NiX zeolites gave current densities of 0.350 and 0.042 mA cm⁻² in 3600 s, respectively.

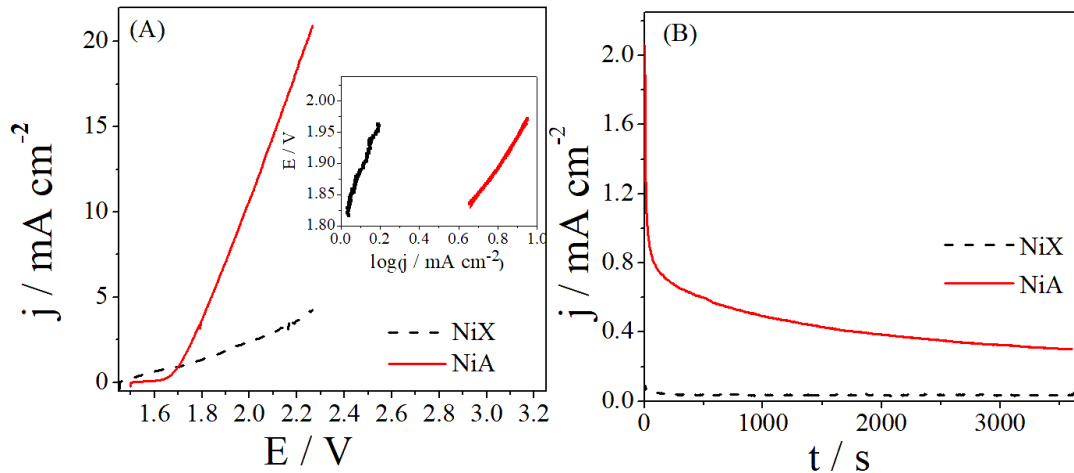


Figure 8. Polarization curves of NiA and NiX electrodes 1 M KOH at 10 mV s⁻¹ and at 1600 rpm with corresponding Tafel plots in inset (A) and chronoamperometric curves at 1.75 V for 3600 s (B).

OER on the Ni-based zeolites was also investigated by EIS. **Figure 9** presents the impedance data at 25 °C (Nyquist and Bode plots) under several applied potentials for the OER at NiA

(**A, C**) and NiX (**B, D**) electrodes. In general, the EIS spectra seems to be controlled by one single relaxation, as suggested by mostly one RC arc in the Nyquist plots and one peak in the Bode plots. The insets of **Figure 9A, B** show the high frequency region of the arcs. However, the Bode plot for OER at NiA (**Figure 9C**) at an applied potential of 1.47 V (the lowest overpotential) shows a second relaxation at low frequencies, which is not so clear for higher overpotentials, where the high frequency contribution is dominating the impedance response. The EIS data was then interpreted by the equivalent circuits of **Figure 10**. The two time constants equivalent circuit in **Figure 10A** was used to fit the data of NiA at 1.47 V, and the one time constant equivalent circuit in **Figure 10B** used for the remaining OER impedance data. Regarding the OER, R_1 may be related to the overall rate of the OER, incorporating the charge transfer resistances of the various steps, while R_2 is again correlated with the formation of intermediates [101,102]. The resistances and capacitances obtained as fitting parameters are presented in **Table 5**.

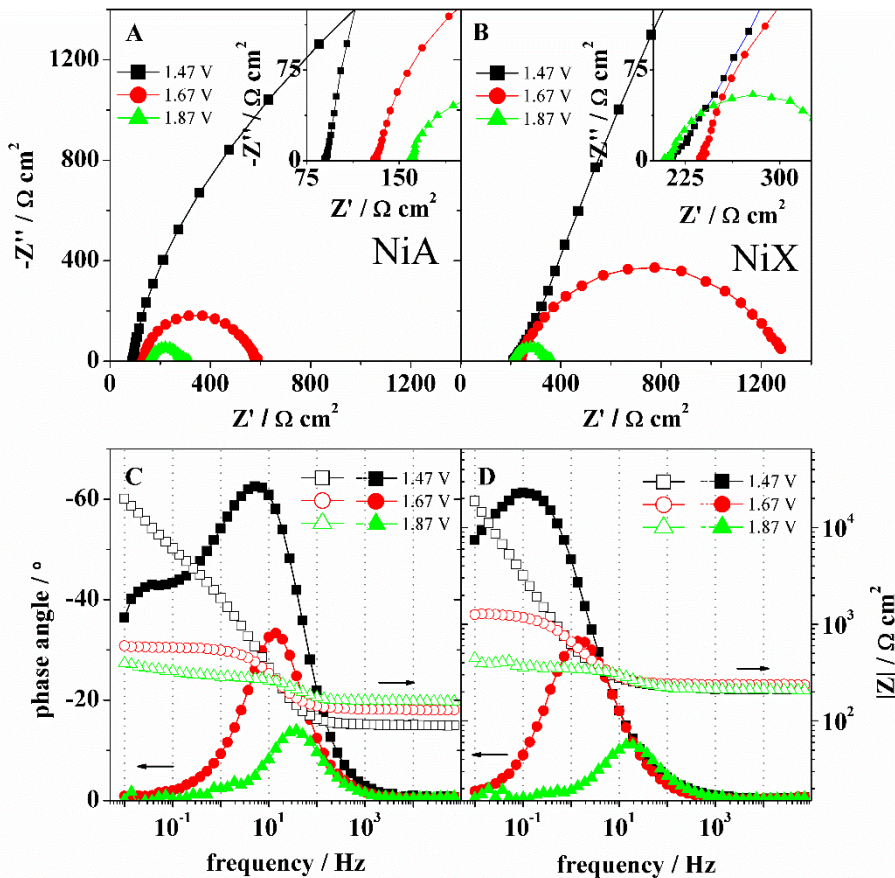


Figure 9. Nyquist ((A, B) and Bode (C, D) plots at several applied potentials for the OER at NiA (A, C) and NiX (B, D) electrocatalysts, at 25 °C.

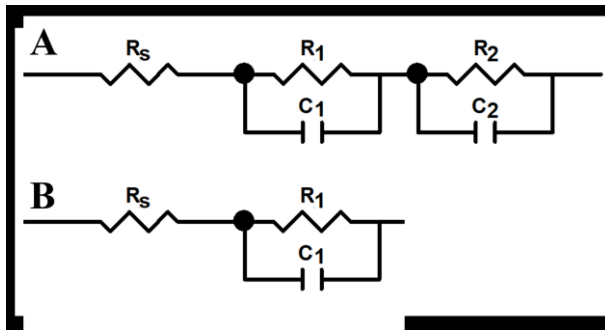


Figure 10. (A) Two time constants equivalent circuit used to fit the data of NiA at 1.47 V, and (B) one time constant equivalent circuit used for the remaining data. R_s is the ohmic resistance of the solution, R_1 and R_2 are resistors, and C_1 and C_2 are capacitors.

Table 5. Parameters obtained from the EIS data at different applied potentials for the OER at NiA and NiX electrocatalysts, at 25 °C.

| $E_{\text{applied}} / \text{V}$ | $R_s / \Omega \text{ cm}^2$ | $R_1 / \Omega \text{ cm}^2$ | $C_1 / \text{F cm}^{-2}$ | $R_2 / \Omega \text{ cm}^2$ | $C_2 / \text{F cm}^{-2}$ |
|---------------------------------|-----------------------------|-----------------------------|--------------------------|-----------------------------|--------------------------|
| NiA | | | | | |
| 1.47 | 93.6 | 2692 ± 156 | 6.6×10^{-5} | 18541 ± 1209 | 4.1×10^{-4} |
| 1.67 | 134.7 | 420 ± 5 | 6.0×10^{-5} | -- | -- |
| 1.87 | 162.1 | 116 ± 1 | 5.0×10^{-5} | -- | -- |
| NiX | | | | | |
| 1.47 | 237.1 | 15182 ± 1505 | 4.0×10^{-4} | -- | -- |
| 1.67 | 247.2 | 923 ± 19 | 2.3×10^{-4} | -- | -- |
| 1.87 | 214.1 | 122 ± 2 | 8.8×10^{-5} | -- | -- |

The values obtained for the electrolyte resistance are much higher in this case than those previously obtained for the HER study, which should be related to some systematic increase of the resistance of the wiring used in the OER measurements and not solely to the electrolyte, since the same electrolyte was used for both HER and OER studies. Nevertheless, higher R_s values were obtained when using NiX electrocatalyst than when NiA was used.

The OER impedance data analysis shows that the charge transfer resistance, R_1 , strongly decreases with increasing overpotential in both cases. Furthermore, these values are lower for NiA than for NiX at all the applied potentials.

Another important aspect is the fact that R_2 , the resistance associated with the lower frequency relaxation, related to the formation of intermediates, which was detected at NiA for applied potential of 1.47 V, is much higher than R_1 , clearly dominating the impedance response. For higher overpotentials, this time constant is absent, and the OER impedance

response is dominated by the charge transfer process itself, which is the opposite of what was observed regarding the HER at NiA.

The capacitance values obtained for the OER are close to the range of expected values for the double layer and the pseudo-capacitance [55,86,91,96]. The capacitance of the double layer, C_1 , shows values of the order of 10^{-5} in the case of NiA and slightly higher (10^{-5} - 10^{-4} F cm $^{-2}$) in the case of NiX, slightly decreasing with the applied potential. These capacitance values are somewhat higher than those observed for the HER. The pseudo-capacitance, C_2 , shows again higher values than C_1 for NiA, as observed for the HER.

4. Conclusion

NiA and NiX zeolites were prepared by ion-exchange method with XRD, FTIR and SEM analysis revealing differences in both structure and morphology of the two zeolites resulting further in difference of their conductivities. Despite a higher degree of amorphisation of NiA zeolite, only one phase was detected by XRD for both synthesized powders. Coherent domain sizes of 47 and 30 nm were obtained for NiX and NiA, respectively, in agreement with a more distorted structure observed for NiA sample after ion-exchange. Zeolites were subsequently studied as electrode materials for HER and OER in alkaline media by LSV, CA and EIS techniques. All electrochemical measurements showed that NiA has higher activity for both studied reactions giving higher current density and lower Tafel slope values than NiX zeolite. At room temperature, Tafel slopes of 463 and 842 mV dec $^{-1}$ were obtained for OER at NiA and NiX zeolites, respectively, while in the case of HER, these slopes amounted to 551 and 857 mV dec $^{-1}$ at 25°C. Chronoamperometric measurements revealed relatively good stability of both zeolites during HER and OER. Analysis of the impedance data revealed that the HER is controlled by the adsorption of the H_{ads} intermediate in the case of NiA, while the overall resistance related to the HER is lower for NiA than for NiX. On the other hand, in the case of the OER, the impedance response is controlled by the charge transfer.

Acknowledgements

The authors would like to thank the Ministry of Education, Science and Technological Development of the Republic of Serbia for support within the project no. OI172043, OI172015 and III45014. The authors would also like to thank Fundação para a Ciência e Tecnologia (FCT, Portugal) for postdoctoral research grant SFRH/BPD/97453/2013 (L. Amaral).

References

- [1] Chi J, Yu H. Water electrolysis based on renewable energy for hydrogen production. *Chinese Journal of Catalysis* 2018;39:390–4. doi:10.1016/S1872-2067(17)62949-8.
- [2] Buttler A, Sliethoff H. Current status of water electrolysis for energy storage, grid balancing and sector coupling via power-to-gas and power-to-liquids: A review. *Renewable and Sustainable Energy Reviews* 2018;82:2440–54. doi:10.1016/j.rser.2017.09.003.
- [3] Santos DMF, Šljukić B, Sequeira CAC, Macciò D, Saccone A, Figueiredo JL. Electrocatalytic approach for the efficiency increase of electrolytic hydrogen production: Proof-of-concept using platinum--dysprosium alloys. *Energy* 2013;50:486–92. doi:10.1016/j.energy.2012.11.003.
- [4] Tahir M, Pan L, Idrees F, Zhang X, Wang L, Zou JJ, et al. Electrocatalytic oxygen evolution reaction for energy conversion and storage: A comprehensive review. *Nano Energy* 2017;37:136–57. doi:10.1016/j.nanoen.2017.05.022.
- [5] Wang H, Gao L. Recent developments in electrochemical hydrogen evolution reaction. *Current Opinion in Electrochemistry* 2018;7:7–14. doi:10.1016/j.coelec.2017.10.010.
- [6] Saba SM, Müller M, Robinius M, Stolten D. The investment costs of electrolysis – A comparison of cost studies from the past 30 years. *International Journal of Hydrogen Energy* 2018;43:1209–23. doi:10.1016/j.ijhydene.2017.11.115.
- [7] Schmidt O, Gambhir A, Staffell I, Hawkes A, Nelson J, Few S. Future cost and performance of water electrolysis: An expert elicitation study. *International Journal of Hydrogen Energy* 2017;42:30470–92. doi:10.1016/j.ijhydene.2017.10.045.
- [8] Sapountzi FM, Gracia JM, Weststrate CJ, Fredriksson HOA, Niemantsverdriet JW. Electrocatalysts for the generation of hydrogen, oxygen and synthesis gas. *Progress in Energy and Combustion Science* 2017;58:1–35. doi:10.1016/j.pecs.2016.09.001.
- [9] Jamesh MI. Recent progress on earth abundant hydrogen evolution reaction and oxygen evolution reaction bifunctional electrocatalyst for overall water splitting in alkaline media. *Journal of Power Sources* 2016;333:213–36. doi:10.1016/j.jpowsour.2016.09.161.
- [10] Xu W, Wang H. Earth-abundant amorphous catalysts for electrolysis of water. *Cuihua Xuebao/Chinese Journal of Catalysis* 2017;38:991–1005. doi:10.1016/S1872-2067(17)62810-9.

- [11] Šljukić B, Vukelić N, Mentus S. Body Ni-doped glassy carbon: Physical and electrochemical characterization. *Materials Science Forum* 2004;453–454:103–8. doi:10.4028.
- [12] Marini S, Salvi P, Nelli P, Pesenti R, Villa M, Berrettoni M, et al. Advanced alkaline water electrolysis. *Electrochimica Acta* 2012;82:384–91. doi:10.1016/j.electacta.2012.05.011.
- [13] Strmcnik D, Lopes PP, Genorio B, Stamenkovic VR, Markovic NM. Design principles for hydrogen evolution reaction catalyst materials. *Nano Energy* 2016;29:29–36. doi:10.1016/j.nanoen.2016.04.017.
- [14] Greeley J, Jaramillo TF, Bonde J, Chorkendorff I, Nørskov JK. Computational high-throughput screening of electrocatalytic materials for hydrogen evolution. *Nature Materials* 2006;5:909–13. doi:10.1038/nmat1752.
- [15] Safizadeh F, Ghali E, Houlachi G. Electrocatalysis developments for hydrogen evolution reaction in alkaline solutions - A Review. *International Journal of Hydrogen Energy* 2015;40:256–74. doi:10.1016/j.ijhydene.2014.10.109.
- [16] Eftekhari A. Electrocatalysts for hydrogen evolution reaction. *International Journal of Hydrogen Energy* 2017;42:11053–77. doi:10.1016/j.ijhydene.2017.02.125.
- [17] Xie Z, He P, Du L, Dong F, Dai K, Zhang T. Comparison of four nickel-based electrodes for hydrogen evolution reaction. *Electrochimica Acta* 2013;88:390–4. doi:10.1016/j.electacta.2012.10.057.
- [18] Abbas SA, Iqbal MI, Kim SH, Jung KD. Catalytic Activity of Urchin-like Ni nanoparticles Prepared by Solvothermal Method for Hydrogen Evolution Reaction in Alkaline Solution. *Electrochimica Acta* 2017;227:382–90. doi:10.1016/j.electacta.2017.01.039.
- [19] Wang L, Li Y, Xia M, Li Z, Chen Z, Ma Z, et al. Ni nanoparticles supported on graphene layers: An excellent 3D electrode for hydrogen evolution reaction in alkaline solution. *Journal of Power Sources* 2017;347:220–8. doi:10.1016/j.jpowsour.2017.02.017.
- [20] Schalenbach M, Speck FD, Ledendecker M, Kasian O, Goehl D, Mingers AM, et al. Nickel-molybdenum alloy catalysts for the hydrogen evolution reaction: Activity and stability revised. *Electrochimica Acta* 2017;259:1154–61. doi:10.1016/j.electacta.2017.11.069.
- [21] Zhang Y, Li P, Yang X, Fa W, Ge S. High-efficiency and stable alloyed nickel based electrodes for hydrogen evolution by seawater splitting. *Journal of Alloys and*

- Compounds 2018;732:248–56. doi:10.1016/j.jallcom.2017.10.194.
- [22] Goranova D, Lefterova E, Rashkov R. Electrocatalytic activity of Ni-Mo-Cu and Ni-Co-Cu alloys for hydrogen evolution reaction in alkaline medium. International Journal of Hydrogen Energy 2017;42:28777–85. doi:10.1016/j.ijhydene.2017.10.002.
- [23] Ahn SH, Park HY, Choi I, Yoo SJ, Hwang SJ, Kim HJ, et al. Electrochemically fabricated NiCu alloy catalysts for hydrogen production in alkaline water electrolysis. International Journal of Hydrogen Energy 2013;38:13493–501. doi:10.1016/j.ijhydene.2013.07.103.
- [24] Zeng K, Zhang D. Evaluating the effect of surface modifications on Ni based electrodes for alkaline water electrolysis. Fuel 2014;116:692–8. doi:10.1016/j.fuel.2013.08.070.
- [25] Sivanantham A, Shanmugam S. Nickel selenide supported on nickel foam as an efficient and durable non-precious electrocatalyst for the alkaline water electrolysis. Applied Catalysis B: Environmental 2017;203:485–93. doi:10.1016/j.apcatb.2016.10.050.
- [26] Cardoso DSP, Amaral L, Santos DMF, Šljukić B, Sequeira CAC, Macciò D, et al. Enhancement of hydrogen evolution in alkaline water electrolysis by using nickel-rare earth alloys. International Journal of Hydrogen Energy 2015;40:4295–302. doi:10.1016/j.ijhydene.2015.01.174.
- [27] Santos DMF, Amaral L, Sljukić B, Macciò D, Saccone A, Sequeira CAC. Electrocatalytic Activity of Nickel-Cerium Alloys for Hydrogen Evolution in Alkaline Water Electrolysis. Journal of The Electrochemical Society 2014;161:386–90. doi:10.1149/2.016404jes.
- [28] Domínguez-Crespo MA, Torres-Huerta AM, Brachetti-Sibaja B, Flores-Vela A. Electrochemical performance of Ni-RE (RE = rare earth) as electrode material for hydrogen evolution reaction in alkaline medium. International Journal of Hydrogen Energy 2011;36:135–51. doi:10.1016/j.ijhydene.2010.09.064.
- [29] Han Q, Liu K, Chen J, Wei X. A study on the electrodeposited Ni-S alloys as hydrogen evolution reaction cathodes. International Journal of Hydrogen Energy 2003;28:1207–12. doi:10.1016/S0360-3199(02)00283-5.
- [30] Cardoso DSP, Eugénio S, Silva TM, Santos DMF, Sequeira CAC, Montemor MF. Hydrogen evolution on nanostructured Ni–Cu foams. RSC Adv 2015;5:43456–61. doi:10.1039/C5RA06517H.
- [31] Mahale NK, Ingle ST. Electrocatalytic hydrogen evolution reaction on nano-nickel

- decorated graphene electrode. Energy 2017;119:872–8. doi:10.1016/j.energy.2016.11.053.
- [32] Popczun EJ, McKone JR, Read CG, Biacchi AJ, Wiltrot AM, Lewis NS, et al. Nanostructured nickel phosphide as an electrocatalyst for the hydrogen evolution reaction. *Journal of the American Chemical Society* 2013;135:9267–70. doi:10.1021/ja403440e.
- [33] Gong M, Zhou W, Tsai M-C, Zhou J, Guan M, Lin M-C, et al. Nanoscale nickel oxide/nickel heterostructures for active hydrogen evolution electrocatalysis. *Nature Communications* 2014;5:1–6. doi:10.1038/ncomms5695.
- [34] Mukherjee A, Chakrabarty S, Su WN, Basu S. Nanostructured nickel ferrite embedded in reduced graphene oxide for electrocatalytic hydrogen evolution reaction. *Materials Today Energy* 2018;8:118–24. doi:10.1016/j.mtener.2018.03.004.
- [35] Jiang N, Tang Q, Sheng M, You B, Jiang D, Sun Y. Nickel sulfides for electrocatalytic hydrogen evolution under alkaline conditions: a case study of crystalline NiS, NiS₂, and Ni₃S₂ nanoparticles. *Catal Sci Technol* 2016;6:1077–84. doi:10.1039/C5CY01111F.
- [36] Laursen AB, Patraju KR, Whitaker MJ, Retuerto M, Sarkar T, Yao N, et al. Nanocrystalline Ni₅P₄: A hydrogen evolution electrocatalyst of exceptional efficiency in both alkaline and acidic media. *Energy and Environmental Science* 2015;8:1027–34. doi:10.1039/c4ee02940b.
- [37] Liu T, Li M, Jiao C, Hassan M, Bo X, Zhou M, et al. Design and synthesis of integrally structured Ni₃N nanosheets/carbon microfibers/Ni₃N nanosheets for efficient full water splitting catalysis. *J Mater Chem A* 2017;5:9377–90. doi:10.1039/C7TA02217D.
- [38] Xing Z, Li Q, Wang D, Yang X, Sun X. Self-supported nickel nitride as an efficient high-performance three-dimensional cathode for the alkaline hydrogen evolution reaction. *Electrochimica Acta* 2016;191:841–5. doi:10.1016/j.electacta.2015.12.174.
- [39] Ma Z, Li Z, Li S, Li P, Zhang H. Nanostructured Ni₂N thin films magnetron-sputtered on nickel foam as efficient electrocatalyst for hydrogen evolution reaction. *Materials Letters* 2018;229:148–51. doi:10.1016/j.matlet.2018.07.016.
- [40] Zhao W, Li M, Wu H, Feng C, Zhang G. Rod-like nonstoichiometric Ni_{0.85}Se as efficient electrocatalysts for hydrogen evolution reaction. *International Journal of Hydrogen Energy* 2018;43:12653–60. doi:10.1016/j.ijhydene.2018.04.123.
- [41] Cheng Y, Jiang SP. Advances in electrocatalysts for oxygen evolution reaction of water electrolysis-from metal oxides to carbon nanotubes. *Progress in Natural Science:*

Materials International 2015;25:545–53. doi:10.1016/j.pnsc.2015.11.008.

- [42] Wang Z, Zhang L. In situ growth of NiTe nanosheet film on nickel foam as electrocatalyst for oxygen evolution reaction. *Electrochemistry Communications* 2018;88:29–33. doi:10.1016/j.elecom.2018.01.014.
- [43] Wang T, Xu W, Wang H. Ternary NiCoFe Layered Double Hydroxide Nanosheets Synthesized by Cation Exchange Reaction for Oxygen Evolution Reaction. *Electrochimica Acta* 2017;257:118–27. doi:10.1016/j.electacta.2017.10.074.
- [44] Hu J, Chen J, Lin H, Liu R, Yang X. MOF derived Ni/Co/NC catalysts with enhanced properties for oxygen evolution reaction. *Journal of Solid State Chemistry* 2018;259:1–4. doi:10.1016/j.jssc.2017.12.030.
- [45] Wang Z, Li M, Fan L, Han J, Xiong Y. Fe/Ni-N-CNFs electrochemical catalyst for oxygen reduction reaction/oxygen evolution reaction in alkaline media. *Applied Surface Science* 2017;401:89–99. doi:10.1016/j.apsusc.2016.12.242.
- [46] Ju H, Li Z, Xu Y. Electro-catalytic activity of Ni-Co-based catalysts for oxygen evolution reaction. *Materials Research Bulletin* 2015;64:171–4. doi:10.1016/j.materresbull.2014.12.063.
- [47] Sequeira CAC, Cardoso DSP, Amaral L, Šljukić B, Santos DMF. On the performance of commercially available corrosion-resistant nickel alloys: A review. *Corrosion Reviews* 2016;34:187–200. doi:10.1515/correv-2016-0014.
- [48] Jiang J, Lu S, Wang WK, Huang GX, Huang BC, Zhang F, et al. Ultrahigh electrocatalytic oxygen evolution by iron-nickel sulfide nanosheets/reduced graphene oxide nanohybrids with an optimized autoxidation process. *Nano Energy* 2018;43:300–9. doi:10.1016/j.nanoen.2017.11.049.
- [49] Zhang C, Xie Y, Deng H, Zhang C, Su JW, Dong Y, et al. Ternary nickel iron phosphide supported on nickel foam as a high-efficiency electrocatalyst for overall water splitting. *International Journal of Hydrogen Energy* 2018;43:7299–306. doi:10.1016/j.ijhydene.2018.02.157.
- [50] Shalom M, Ressnig D, Yang X, Clavel G, Fellinger TP, Antonietti M. Nickel nitride as an efficient electrocatalyst for water splitting. *Journal of Materials Chemistry A* 2015;3:8171–7. doi:10.1039/c5ta00078e.
- [51] Swesi AT, Masud J, Nath M. Nickel selenide as a high-efficiency catalyst for oxygen evolution reaction. *Energy and Environmental Science* 2016;9:1771–82. doi:10.1039/c5ee02463c.
- [52] Xu X, Song F, Hu X. A nickel iron diselenide-derived efficient oxygen-evolution

- catalyst. *Nature Communications* 2016;7:1–7. doi:10.1038/ncomms12324.
- [53] Xie Y, Liu H, Hu N. Layer-by-layer films of hemoglobin or myoglobin assembled with zeolite particles: Electrochemistry and electrocatalysis. *Bioelectrochemistry* 2007;70:311–9. doi:10.1016/j.bioelechem.2006.04.002.
- [54] Jović A, Đorđević A, Čebela M, Stojković Simatović I, Hercigonja R, Šljukić B. Composite zeolite/carbonized polyaniline electrodes for p-nitrophenol sensing. *Journal of Electroanalytical Chemistry* 2016;778:137–147. doi:10.1016/j.jelechem.2016.08.025.
- [55] Vasić M, Čebela M, Pašti I, Amaral L, Hercigonja R, Santos DMF, et al. Efficient hydrogen evolution electrocatalysis in alkaline medium using Pd-modified zeolite X. *Electrochimica Acta* 2018;259:882–92. doi:10.1016/j.electacta.2017.11.020.
- [56] Ania CO, Khomenko V, Raymundo-Piñero E, Parra JB, Béguin F. The large electrochemical capacitance of microporous doped carbon obtained by using a zeolite template. *Advanced Functional Materials* 2007;17:1828–36. doi:10.1002/adfm.200600961.
- [57] Mojović Z, Banković P, Jović-Jovičić N, Milutinović-Nikolić A, Abu Rabi-Stanković A, Jovanović D. Electrocatalytic behavior of nickel impregnated zeolite electrode. *International Journal of Hydrogen Energy* 2011;36:13343–51. doi:10.1016/j.ijhydene.2011.07.097.
- [58] Li G, Yu H, Song W, Wang X, Li Y, Shao Z, et al. Zeolite-templated $\text{Ir}_x\text{Ru}_{1-x}\text{O}_2$ electrocatalysts for oxygen evolution reaction in solid polymer electrolyte water electrolyzers. *International Journal of Hydrogen Energy* 2012;37:16786–94. doi:10.1016/j.ijhydene.2012.08.087.
- [59] Oliveira RCP, Vasić M, Santos DMF, Babić B, Hercigonja R, Sequeira CAC, et al. Performance assessment of a direct borohydride-peroxide fuel cell with Pd-impregnated faujasite X zeolite as anode electrocatalyst. *Electrochimica Acta* 2018;269:517–25. doi:10.1016/j.electacta.2018.03.021.
- [60] Medina Ramírez A, Villicaña Aguilera M, López-Badillo CM, Ruiz-Camacho B. Synthesis of FAU zeolite-C composite as catalyst support for methanol electro-oxidation. *International Journal of Hydrogen Energy* 2017;42:30291–300. doi:10.1016/j.ijhydene.2017.08.172.
- [61] Azizi SN, Ghasemi S, Gilani NS. An electrode with Ni(II) loaded analcime zeolite catalyst for the electrooxidation of methanol. *Chinese Journal of Catalysis* 2014;35:383–90. doi:10.1016/S1872-2067(14)60002-4.

- [62] Azizi SN, Ghasemi S, Amiripour F. A new attitude to environment: Preparation of an efficient electrocatalyst for methanol oxidation based on Ni-doped P zeolite nanoparticles synthesized from stem sweep ash. *Electrochimica Acta* 2014;137:395–403. doi:10.1016/j.electacta.2014.05.158.
- [63] Raoof JB, Azizi N, Ojani R, Ghodrati S, Abrishamkar M, Chekin F. Synthesis of ZSM-5 zeolite: Electrochemical behavior of carbon paste electrode modified with Ni (II)-zeolite and its application for electrocatalytic oxidation of methanol. *International Journal of Hydrogen Energy* 2011;36:13295–300. doi:10.1016/j.ijhydene.2010.06.055.
- [64] Eftekhari A. Tuning the electrocatalysts for oxygen evolution reaction. *Materials Today Energy* 2017;5:37–57. doi:10.1016/j.mtener.2017.05.002.
- [65] Polat E, Karaca M, Demir H, Onus a N. Use of natural zeolite (clinoptilolite) in agriculture. *Journal of Fruit and Ornamental Plant Reserarch* 2004;12:183–9.
- [66] Valdes MG, Perez-Cordoves AI, Diaz-Garcia ME. Zeolites and zeolite-based materials in analytical chemistry. *TrAC - Trends in Analytical Chemistry* 2006;25:24–30. doi:10.1016/j.trac.2005.04.016.
- [67] Inokawa H, Maeda M, Nishimoto S, Kameshima Y, Miyake M, Ichikawa T, et al. Synthesis of nickel nanoparticles with excellent thermal stability in micropores of zeolite. *International Journal of Hydrogen Energy* 2013;38:13579–86. doi:10.1016/j.ijhydene.2013.08.027.
- [68] Cheary RW, Coelho A. Fundamental parameters approach to x-ray line-profile fitting. *Journal of Applied Crystallography* 1992;25:109–21. doi:10.1107/S0021889891010804.
- [69] Coutinho D, Balkus KJ. Preparation and characterization of zeolite X membranes via pulsed-laser deposition. *Microporous and Mesoporous Materials* 2002;52:79–91. doi:10.1016/S1387-1811(02)00273-1.
- [70] Aronne A, Esposito S, Ferone C, Pernice P, Federico N, Tecchio IIP, et al. FTIR study of the thermal transformation of barium-exchanged zeolite A to celsian. *Journal of Materials Chemistry* 2002;12:3039–45. doi:10.1039/b203859e.
- [71] Baerlocher C, Meier WM, Olson DH. *Atlas of Zeolite Framework Types*. Amsterdam: Elsevier; 2001.
- [72] Yang X, Albrecht D, Caro J. Revision of Charnell's procedure towards the synthesis of large and uniform crystals of zeolites A and X. *Microporous and Mesoporous Materials* 2006;90:53–61. doi:10.1016/j.micromeso.2005.10.044.
- [73] Rutter M., Secco R., Huang Y. Ionic conduction in hydrated zeolite Li-, Na- and K-A

- at high pressures. *Chemical Physics Letters* 2000;331:189–95. doi:10.1016/S0009-2614(00)01191-X.
- [74] Hahn F, Floner D, Beden B, Lamy C. In situ investigation of the behaviour of a nickel electrode in alkaline solution by uv-vis and ir reflectance spectroscopies. *Electrochimica Acta* 1987;32:1631–6. doi:10.1016/0013-4686(87)90016-8.
- [75] Santos DMF, Amaral L, Sljukić B, Maccio D, Saccone A, Sequeira CAC. Nickel-Cerium Electrodes for Hydrogen Evolution in Alkaline Water Electrolysis. *ECS Transactions* 2013;58:113–21. doi:10.1149/05802.0113ecst.
- [76] Mojovic Z, Mentus S, Krstic I. Thin layer of Ni-modified 13X zeolite on glassy carbon support as an electrode material in aqueous solutions. *Russian Journal of Physical Chemistry A* 2007;81:1452–7. doi:10.1134/S0036024407090208.
- [77] Kumar JP, Giri SD, Sarkar A. Mesoporous NiO with different morphology: Synthesis, characterization and their evaluation for oxygen evolution reaction. *International Journal of Hydrogen Energy* 2018;1–11. doi:10.1016/j.ijhydene.2018.06.097.
- [78] Kjartansdottir CK, Nielsen LP, Moller P. Development of durable and efficient electrodes for large-scale alkaline water electrolysis. *International Journal of Hydrogen Energy* 2013;38:8221–31. doi:10.1016/j.ijhydene.2013.04.101.
- [79] Birry L, Lasia A. Studies of the hydrogen evolution reaction on Raney nickel-molybdenum electrodes. *Journal of Applied Electrochemistry* 2004;34:735–49. doi:10.1023/B:JACH.0000031161.26544.6a.
- [80] Jakšić JM, Vojnović M V., Krstajić N V. Kinetic analysis of hydrogen evolution at Ni-Mo alloy electrodes. *Electrochimica Acta* 2000;45:4151–8. doi:10.1016/S0013-4686(00)00549-1.
- [81] Łosiewicz B, Budniok A, Rówiński E, Łagiewka E, Lasia A. The structure, morphology and electrochemical impedance study of the hydrogen evolution reaction on the modified nickel electrodes. *International Journal of Hydrogen Energy* 2004;29:145–57. doi:10.1016/S0360-3199(03)00096-X.
- [82] Lasia A, Rami A. Kinetics of hydrogen evolution on nickel electrodes. *Journal of Electroanalytical Chemistry* 1990;294:123–41. doi:10.1016/0022-0728(90)87140-F.
- [83] Šljukić B, Vujković M, Amaral L, Santos DMF, Rocha RP, Sequeira CAC, et al. Carbon-supported Mo₂C electrocatalysts for hydrogen evolution reaction. *J Mater Chem A* 2015;3:15505–12. doi:10.1039/C5TA02346G.
- [84] Chanda D, Hná JR, Dobrota AS, Paš IA, Paidar M, Bouzek K. The effect of surface modification by reduced graphene oxide on the electrocatalytic activity of nickel

- towards the hydrogen evolution reaction. *Phys Chem Chem Phys* 2015;17:26864–74. doi:10.1039/c5cp04238k.
- [85] Soares DM. Hydride Effect on the Kinetics of the Hydrogen Evolution Reaction on Nickel Cathodes in Alkaline Media. *Journal of The Electrochemical Society* 1992;139:98–105. doi:10.1149/1.2069207.
- [86] Amaral L, Cardoso DSP, Šljukić B, Santos DMF, Sequeira CAC. Room Temperature Ionic Liquids as Electrolyte Additives for the HER in Alkaline Media. *Journal of The Electrochemical Society* 2017;164:F427–32. doi:10.1149/2.0011706jes.
- [87] Šljukić B, Santos DMF, Vujković M, Amaral L, Rocha RP, Sequeira CAC, et al. Molybdenum Carbide Nanoparticles on Carbon Nanotubes and Carbon Xerogel: Low-Cost Cathodes for Hydrogen Production by Alkaline Water Electrolysis. *ChemSusChem* 2016;9(10):1200–8. doi:10.1002/cssc.201501651.
- [88] Brug GJ, van den Eeden ALG, Sluyters-Rehbach M, Sluyters JH. The analysis of electrode impedances complicated by the presence of a constant phase element. *Journal of Electroanalytical Chemistry* 1984;176:275–95. doi:10.1016/S0022-0728(84)80324-1.
- [89] Rammelt U, Reinhard G. On the applicability of a constant phase element (CPE) to the estimation of roughness of solid metal electrodes. *Electrochimica Acta* 1990;35:1045–9. doi:10.1016/0013-4686(90)90040-7.
- [90] Amaral L, Cardoso DSP, Šljukić B, Santos DMF, Sequeira CAC. Electrochemistry of hydrogen evolution in RTILs aqueous mixtures. *Materials Research Bulletin* 2018;1–26. doi:10.1016/j.materresbull.2018.04.041.
- [91] Franceschini EA, Lacconi GI, Corti HR. Kinetics of the hydrogen evolution on nickel in alkaline solution: New insight from rotating disk electrode and impedance spectroscopy analysis. *Electrochimica Acta* 2015;159:210–8. doi:10.1016/j.electacta.2015.01.110.
- [92] Krstajić N, Popović M, Grgur B, Vojnović M, Šepa D. On the kinetics of the hydrogen evolution reaction on nickel in alkaline solution - Part I. The mechanism. *Journal of Electroanalytical Chemistry* 2001;512:16–26. doi:10.1016/S0022-0728(01)00590-3.
- [93] Armstrong RD, Henderson M. Impedance plane display of a reaction with an adsorbed intermediate. *Electroanalytical Chemistry and Interfacial Electrochemistry* 1972;39:81–90.
- [94] Navarro-Flores E, Chong Z, Omanovic S. Characterization of Ni, NiMo, NiW and NiFe electroactive coatings as electrocatalysts for hydrogen evolution in an acidic

- medium. *Journal of Molecular Catalysis A: Chemical* 2005;226:179–97. doi:10.1016/j.molcata.2004.10.029.
- [95] Sequeira CAC, Santos DMF, Šljukić B, Amaral L. Physics of Electrolytic Gas Evolution. *Brazilian Journal of Physics* 2013;43:199–208. doi:10.1007/s13538-013-0131-4.
- [96] Bai L, Harrington DA, Conway BE. Behavior of overpotential-deposited species in Faradaic reactions-II. ac Impedance measurements on H₂ evolution kinetics at activated and unactivated Pt cathodes. *Electrochimica Acta* 1987;32:1713–31. doi:10.1016/0013-4686(87)80006-3.
- [97] Zhou W, Wu X-J, Cao X, Huang X, Tan C, Tian J, et al. Ni₃S₂ nanorods/Ni foam composite electrode with low overpotential for electrocatalytic oxygen evolution. *Energy & Environmental Science* 2013;6:2921–4. doi:10.1039/c3ee41572d.
- [98] Ponce J, Rehspringer JL, Poillerat G, Gautier JL. Electrochemical study of nickel-aluminium-manganese spinel NixAl_{1-x}Mn₂O₄. Electrocatalytical properties for the oxygen evolution reaction and oxygen reduction reaction in alkaline media. *Electrochimica Acta* 2001;46:3373–80. doi:10.1016/S0013-4686(01)00530-8.
- [99] Ding Y, Li H, Hou Y. Robust polyoxometalate-loaded nickel foam for electrocatalytic oxygen evolution reaction. *Materials Letters* 2018;221:264–6. doi:10.1016/j.matlet.2018.03.133.
- [100] Zhang Y, Cao X, Yuan H, Zhang W, Zhou Z. Oxygen evolution reaction on Ni hydroxide film electrode containing various content of Co. *International Journal of Hydrogen Energy* 1999;24:529–36. doi:10.1016/S0360-3199(98)00086-X.
- [101] Swierk JR, Klaus S, Trotochaud L, Bell AT, Tilley TD. Electrochemical Study of the Energetics of the Oxygen Evolution Reaction at Nickel Iron (Oxy)Hydroxide Catalysts. *The Journal of Physical Chemistry C* 2015;119:19022–9. doi:10.1021/acs.jpcc.5b05861.
- [102] Doyle RL, Lyons MEG. An electrochemical impedance study of the oxygen evolution reaction at hydrous iron oxide in base. *Physical Chemistry Chemical Physics* 2013;15:5224–37. doi:10.1039/c3cp43464h.